PCCP

ROYAL SOCIETY OF CHEMISTRY

PAPER

View Article Online
View Journal | View Issue

Cite this: *Phys. Chem. Chem. Phys.*, 2024, **26**, 6325

Chemical engineering of cationic distribution in spinel ferrite nanoparticles: the effect on the magnetic properties†

Miran Baričić, ‡*[a] Pierfrancesco Maltoni, *[b] Gianni Barucca, [c] Nader Yaacoub,[d] Alexander Omelyanchik, [ae] Fabio Canepa, [a] Roland Mathieu [b] and Davide Peddis *[ae]

Received 11th December 2023,
Accepted 16th January 2024

DOI: 10.1039/d3cp06029b

rsc.li/pccp

A set of ~9 nm $CoFe_2O_4$ nanoparticles substituted with Zn^{2+} and Ni^{2+} was prepared by thermal decomposition of metallic acetylacetonate precursors to correlate the effects of replacement of Co^{2+} with the resulting magnetic properties. Due to the distinct selectivity of these cations for the spinel ferrite crystal sites, we show that it is possible to tailor the magnetic anisotropy, saturation magnetization, and interparticle interactions of the nanoparticles during the synthesis stage. This approach unlocks new possibilities for enhancing the performance of spinel ferrite nanoparticles in specific applications. Particularly, our study shows that the replacement of Co^{2+} by 48% of Zn^{2+} ions led to an increase in saturation magnetization of approximately 40% from ~103 A m^2 kg^{-1} to ~143 A m^2 kg^{-1}, whereas the addition of Ni^{2+} at a similar percentage led to an ~30% decrease in saturation magnetization to 68–72 A m^2 kg^{-1}. The results of calculations based on the two-sublattice Néel model of magnetization match the experimental findings, demonstrating the model's effectiveness in the strategic design of spinel ferrite nanoparticles with targeted magnetic properties through doping/inversion degree engineering.

Introduction

Spinel ferrites are materials with stoichiometry $M^{2+}Fe_2O_4$ (M^{2+} = Co^{2+}, Zn^{2+}, Ni^{2+}, Fe^{2+}) that have been intensely studied for their chemical flexibility, enabling the inclusion of a wide range of transition metal cations, thus providing an easy way to tune their magnetic properties. For these reasons, spinel ferrite nanoparticles (NPs) are suitable for many applications such as MRI contrast agents,[1–3] molecular detection and separation, drug delivery systems and hyperthermic therapy,[4,5] and design of rare-earth-free permanent magnets.[6–11]

The spinel ferrite structure consists of a cubic close-packed (ccp) arrangement of oxygen atoms with tetrahedral (T_d) and octahedral [O_h] sites.[12–14] The cationic distribution is often reported as $(M_{1-\delta}{}^{2+}Fe_{\delta}{}^{3+})_{T_d}[M_{\delta}{}^{2+}Fe_{2-\delta}{}^{3+}]_{O_h}O_4$, with δ as the inversion degree, with a value between 0 (in normal spinel and 1 (in inverse spinel). The magnetization of spinel ferrites can be described by Néel's model for antiferro- and ferrimagnetic materials,[12,13,15] where the total magnetic moment is the vectorial sum of the magnetic sublattice's magnetizations, corresponding to O_h and T_d sites in spinel ferrites: $\mu_{tot} = \sum \mu_{O_h} - \sum \mu_{T_d}$.

Since the metallic cations have different magnetic properties and site selectivity within the lattice, such spinel structures offer the possibility to easily modify the saturation magnetization (M_s), magneto-crystalline anisotropy, and interparticle magnetic interactions. Specifically, cobalt ferrite is a relatively highly anisotropic material with δ values in the range of 0.66 to 0.8;[13,16–19] its large magneto-crystalline anisotropy (K_1 = 290 kJ m^{-3} at room temperature[20]) is due to the strong single-ion anisotropy of Co^{2+} in O_h-sites, arising from its non-quenched spin–orbit coupling.[21] Ni^{2+} and Zn^{2+} exhibit lower

[a] *Dipartimento di Chimica e Chimica Industriale & INSTM, nM2-Lab, Università degli Studi di Genova, Via Dodecaneso 31, Genova, 1-16146, Italy. E-mail: miranbaricic@yahoo.com, davide.peddis@unige.it*
[b] *Department of Materials Science and Engineering, Uppsala University, Box 35, Uppsala, 751 03, Sweden. E-mail: pierfrancesco.maltoni@angstrom.uu.se*
[c] *Dipartimento di Scienze e Ingegneria della Materia, Dell'ambiente ed Urbanistica, Università Politecnica delle Marche, via Brecce Bianche 12, Ancona, Italy*
[d] *Institut des Molécules et Matériaux du Mans, CNRS UMR-6283, Le Mans Université, F-72085 Le Mans, France*
[e] *Institute of Structure of Matter (ISM), nM2-Lab, National Research Council (CNR), Via Salaria, Km 29,300 00015 Monterotondo Scalo, Roma, Italy*

† Electronic supplementary information (ESI) available. See DOI: https://doi.org/10.1039/d3cp06029b

‡ Present affiliations: Laboratoire Interfaces Traitements Organisation et Dynamique des Systèmes, Université Paris Cité, CNRS UMR-7886, Rue Jean Antoine de Baïf, 75013 Paris, France and Dipartimento di Scienze, Università degli Studi Roma TRE, Via della Vasca Navale, 84-00146 Roma, Italy.

anisotropy in comparison to Co^{2+}, yet—owing to their different single-ion properties and site selectivity—they yield opposite effects on saturation magnetization, providing interesting perspectives. Ni^{2+} tends to occupy the O_h sites, while Zn^{2+} prefers T_d sites.[11,22,23] The selectivity for different sites leads to a change in the inversion degree of the spinel structure.

When Ni^{2+} substitutes Co^{2+}, the inversion degree increases (*i.e.*, the stoichiometric $NiFe_2O_4$ is the totally inverted spinel with $\delta = 1$) while Zn^{2+} substitution leads to a lower value of δ.[24] This ability to control the inversion degree by chemical engineering provides an additional degree of freedom in designing the magnetic properties of spinel ferrite NPs.

At the nanoscale, the magnetic structure of spinel ferrites is due to the complex interplay between cationic distribution and surface magnetic disorder (*i.e.*, spin canting[25]) as well as it is related to the particle size and synthesis method.[24] For example, Mameli *et al.*[26] studied the magnetic properties of $\sim$7 nm Zn-substituted $CoFe_2O_4$ NPs and reported a reduction of inversion degree to $\sim$0.4 when the Zn^{2+} content was $\sim$0.5. This led to a significant enhancement in saturation magnetisation up to 157 ± 3 A m^2 kg^{-1}, which is higher than the value measured for pure $CoFe_2O_4$. Andersen *et al.*[27] found metastable cation distributions in hydrothermally prepared Zn-substituted $CoFe_2O_4$ NPs leading to increased M_s in Zn-rich samples, which decreased after annealing to the thermodynamic distribution.

On the other hand, nanocrystals of $NiFe_2O_4$ and $CoFe_2O_4$ may exhibit weak interdependence between particle size and inversion degree. For example, in their study, Carta *et al.*[16] demonstrated that 6–9 nm NPs (including cobalt and nickel ferrites) prepared by the sol–gel method show the same inversion degree values as bulk analogues (0.68 and 1.0, respectively). On the other hand, Muscas *et al.*[28] reported values of $\sim$0.74, $\sim$0.78, and $\sim$0.44 for $CoFe_2O_4$, $Ni_{0.5}Co_{0.5}Fe_2O_4$, and $NiFe_2O_4$ NPs of $\sim$4.5 nm, respectively, significantly different from bulk.

In this framework, comparative studies of nanostructure spinel ferrites, which go beyond the effect of synthesis methods and morpho structural features, appear to be very important. To the best of our knowledge, no prior studies have directly compared Zn- and Ni-substituted $CoFe_2O_4$ NPs synthesized by the same method and with comparable morpho-structural features.

This study focuses on the comparative study of magnetic properties of $M_xCo_{1-x}Fe_2O_4$ ($M^{2+} = Ni^{2+}$, Zn^{2+}) NPs with increasing Ni^{2+}/Zn^{2+} content. The thermal decomposition of metallic acetylacetonates in high-temperature boiling solvent (TD) synthesis[29] has been used to have a fine control on morpho-structural features of NPs and the high value of M_s (see Fig. S1, ESI†). Furthermore, to the best of our knowledge, a few studies of the low-temperature magnetic properties of $M_xCo_{1-x}Fe_2O_4$ are available in the literature[28,30,31] (see Fig. S1a, ESI†).[32–34] We prepared two sets of samples (hereafter referred to as "Ni-series" and "Zn-series") which have an increasing M^{2+} substitution with respect to the cobalt-ferrite reference sample. The NPs have comparable size and shape distributions, thus avoiding any possible size effects on the magnetic properties owing to changes in the inversion degree.[19] Therefore, this system can be considered as a model that allows us to establish direct correlations between the magnetic structure (*i.e.*, cationic distribution) and magnetic properties. Herein, we present a thorough investigation, conducted at both low temperature and room temperature, on the magnetic anisotropy, saturation magnetization, and interparticle interactions. Inversion/doping content maps of the low temperature M_s were plotted by considering a spin-only two-sublattice Néel model of magnetization. The usefulness of the maps is demonstrated by predicting M_s for 2 samples for the Ni- and Zn-series with known composition and cationic distribution from in-field Mössbauer spectrometry. The potential interest of this study is related to the possibility of controlling the magnetic structure at the nanoscale, opening interesting perspectives to improve materials' performance for targeted technological applications.

Experimental methods

Synthesis

For the synthesis of $\sim$9 nm $CoFe_2O_4$ NPs, $Fe(acac)_3$ (2 mmol), $Co(acac)_2$ (1 mmol), oleic acid (OLAC, 6 mmol), oleylamine (OLAM, 6 mmol), 1,2-hexadecanediol (HDD, 10 mmol) and dibenzylether (DBE, 20 mL) were employed according to the method described by Sun *et al.*[29] All chemicals were stirred under an inert nitrogen atmosphere at 200 °C for 2 h, and then at 300 °C for 1 h (heating rates 5 °C min^{-1}); at the end of the thermal program, the product was cooled at room temperature by removing the heating mantle. Eventually, the sample was washed in ethanol using a centrifuge (10 min, 4000 rpm) three times, and stored in a few mL of toluene. To synthesize $M_xCo_{1-x}Fe_2O_4$ ($M^{2+} = Ni^{2+}$, Zn^{2+}), $Co(acac)_2$ was partially substituted with $Ni(acac)_2$ or $Zn(acac)_2$, so that the sum of all Co^{2+} and M^{2+} acetylacetonates is kept to 1 mmol. The resulting stoichiometries in the final product were analysed by inductively coupled plasma atomic emission spectroscopy (ICP-AES), and each sample was named after its M^{2+} stoichiometric coefficient, x (*e.g.*, Zn19 or Ni63). The samples were all compared with a reference no-substituted sample, CoRef. See the used acronyms of samples in Table 1.

Characterization techniques

X-ray powder diffraction (XRPD) was performed on NP powders using a Bruker D8 Advance diffractometer (solid state LynxEye detector, Cu Kα radiation, Bragg Brentano geometry, DIFFRACT

Table 1 Sample acronyms, stoichiometry defined *via* ICP analysis, average XRPD ($\langle d \rangle_{XRPD}$) and TEM ($\langle d \rangle_{TEM}$) diameters

Sample	Stoichiometry	$\langle d \rangle_{XRPD}$, nm	$\langle d \rangle_{TEM}$, nm
CoRef	$Co_{0.85}Fe_{2.15}O_4$	8.3(4)	9.0(1)
Ni22	$Ni_{0.22}Co_{0.71}Fe_{2.07}O_4$	8.0(4)	8.1(1)
Ni39	$Ni_{0.39}Co_{0.45}Fe_{2.16}O_4$	8.3(5)	8.5(1)
Ni63	$Ni_{0.63}Co_{0.23}Fe_{2.14}O_4$	8.3(5)	10.0(1)
Zn19	$Zn_{0.19}Co_{0.70}Fe_{2.11}O_4$	9.3(4)	8.4(2)
Zn32	$Zn_{0.32}Co_{0.47}Fe_{2.22}O_4$	9.0(1)	8.7(1)
Zn48	$Zn_{0.48}Co_{0.26}Fe_{2.26}O_4$	8.6(5)	9.3(2)

plus software). The average sizes of crystallites were calculated using the Scherrer equation.[35] Transmission Electron Microscopy (TEM) images were acquired using a Philips CM200 microscope operating at 200 kV and equipped with a LaB_6 filament. The statistical analysis of particles' sizes was performed using the ImageJ software.[28] Inductively Coupled Plasma – Atomic Emission Spectroscopy (ICP-AES) measurements were performed using an iCAP 6300 DUP ICP-AES spectrometer (ThermoScientific) to check the composition of each sample. Thermo-gravimetric Analysis (TGA) was performed on a LabsysEvo 1600 DTA/TGA (Setaram): a few mg of powder was placed in an alumina crucible and heated from 30 to 1000 °C at 10 °C min^{-1} under an O_2 atmosphere (20 mL min^{-1}). The magnetization was normalized considering the weight loss measured by TGA, due to decomposition of the organic part.

DC magnetization measurements were performed using a SQUID magnetometer (Quantum Design MPMS XL). The field dependence of magnetization loops was measured at 5 and 300 K in the range of ±5 T. The saturation magnetization (M_s) of each sample was obtained by fitting the high field values with the Law of Approach to Saturation (LAS) $M(H) = M_s(1 - a/H - b/H^2)$ where a and b are free-fitting parameters, and H is the applied field.[36] The temperature dependence of magnetization has been investigated using Zero Field Cooled (ZFC) and Field Cooled (FC) protocols under 2.5 mT fields from 5 to 300 K, and T_{max} and T_b were estimated by following the procedure reported in ref. 37. Remanent magnetization was measured by means of Isothermal Remanent Magnetization (IRM) and Direct Current Demagnetization (DCD) protocols.[38,39] IRM curves are obtained starting from a demagnetized sample at $\mu_0 H = 0$ T and measuring the remanence corresponding to increasing fields $\mu_0 H > 0$; DCD curves are obtained in the same manner, but the measurement starts from $\mu_0 H = 0$ with a sample previously being saturated at $\mu_0 H = -5$ T. ^{57}Fe Mössbauer spectra were obtained at 12 K in an externally applied field of 8 T oriented parallel to the γ-beam using a ^{57}Co/Rh γ-ray source mounted on an electromagnetic transducer with a triangular velocity form. The hyperfine structure was modelled by a least-squares fitting procedure involving Zeeman sextets composed of Lorentzian lines using MOSSFIT (made-home software). The isomer shift values δ are referred to those of α-Fe at 300 K.

Results and discussions

The XRPD patterns show the typical reflections of the spinel $Fd\bar{3}m$ cubic phase for all the samples, without any secondary phase (Fig. 1 and Fig. S2, ESI†). The crystallite size obtained by the Scherrer equation and estimated from the analysis of the TEM pictures were found in agreement (Table 1), suggesting the high crystallinity of the samples. TEM images confirm the spherical morphology and the low polydispersity of the particles (ESI,† Section S3; Table 1). It should be emphasized that the size is constant within experimental errors of different samples, allowing the investigation of magnetic properties beyond the effect of NPs' size.[40]

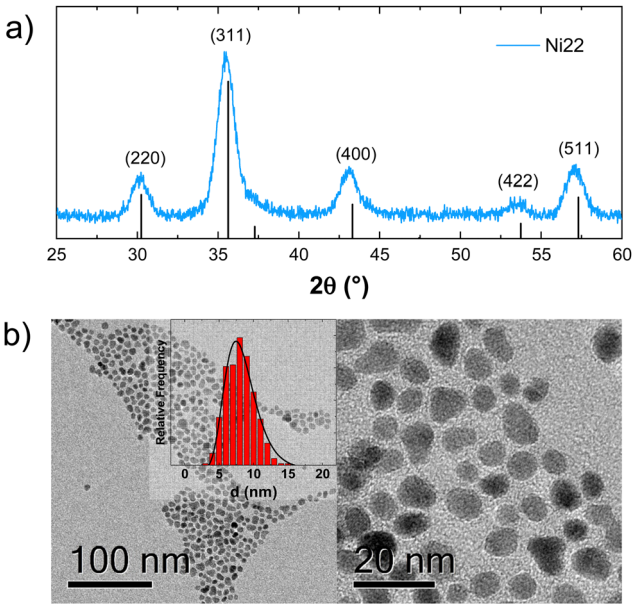

Fig. 1 (a) XRPD pattern and (b) TEM pictures and size distribution histogram of sample Ni22.

TGA was performed to determine the organic content (ESI,† Section S4) and the magnetization measurements were normalised considering only the inorganic content. The ICP analysis revealed an excess of iron with respect to the stoichiometric Co : Fe 1 : 2 ratio (Table 1 and ESI,† Section S5) expected for cobalt ferrite. This phenomenon was already observed for $CoFe_2O_4$ particles by Gyergyek *et al.*[41] made with the same approach, putting forward the lack of Co^{2+} as a consequence of the higher stability of Co^{2+}-oleate, compared to Fe^{3+}-oleate, and attributed the iron excess to the presence of Fe^{2+}. This agrees with other studies, that do not exclude the formation of Fe^{2+}[29,42]. We left out the possibility that the $Fe^{2+/3+}$ excess formed oxide impurities, as we did not identify any, neither structurally nor magnetically, as also observed by Mössbauer spectrometry. Note that, based on the mean value of isomer shift, the recorded spectra on all studied samples do not provide evidence for the presence of Fe^{2+} ions (Table S4 and Fig. S10, ESI†).

The temperature dependence of magnetization recorded by ZFC/FC protocols (Fig. S6, ESI†) shows a clear dependence: the average blocking temperature and temperature of M_{ZFC} maximum (*i.e.*, T_b and T_{max}) decrease with an increase in Ni^{2+} and Zn^{2+} contents, suggesting a dominating effect of the magnetic anisotropy, even if an effect due to interparticle interactions can be present (ESI,† Section S6 and Table 2).[11]

Magnetic anisotropy

The decrease in magnetic anisotropy is also confirmed by the shift in the maximum irreversible susceptibility obtained by the differentiated DCD curves at 5 K ($\chi_{irr} = dM_{DCD}/dH$) (Fig. 2), which is directly correlated with the distribution of coercive fields (*i.e.*, switching fields distribution, SFD). All the SFDs have a single peak shape, indicating a homogeneous magnetization

Table 2 Blocking and maximum temperatures from ZFC/FC (T_b, T_{max}), 5 K switching field ($\mu_0 H_{sw}$), 5 and 300 K magnetic saturation (M_s), reduced remanence (M_r/M_s), coercivity ($\mu_0 H_C$) and anisotropy constant (K_a). Uncertainties on the last digit indicated in parentheses

Sample	T_b, K	T_{max}, K	$\mu_0 H_{sw}$ (5 K), T	M_s (5 K), A m^2 kg^{-1}	M_s (300 K), A m^2 kg^{-1}	M_r/M_s (5 K)	$\mu_0 H_c$ (5 K), T	K_a, 10^{-5} J m^{-3}
CoRef	199(1)	289(1)	1.25(1)	103(2)	85(2)	0.60(3)	1.06(5)	11
Ni22	166(1)	252(1)	1.0(1)	73(1)	58(1)	0.67(1)	0.95(5)	5.7
Ni39	166(1)	228(1)	0.9(1)	68(3)	58(2)	0.68(4)	0.85(4)	4.5
Ni63	107(1)	157(1)	0.6(1)	72(2)	56(2)	0.64(2)	0.51(3)	3.1
Zn19	207(1)	285(1)	0.8(1)	104(3)	80(2)	0.56(3)	0.67(3)	7.1
Zn32	166(1)	228(1)	0.6(1)	114(4)	80(3)	0.56(4)	0.47(2)	5.3
Zn48	132(1)	201(1)	0.3(1)	143(5)	93(3)	0.49(4)	0.27(1)	4.3

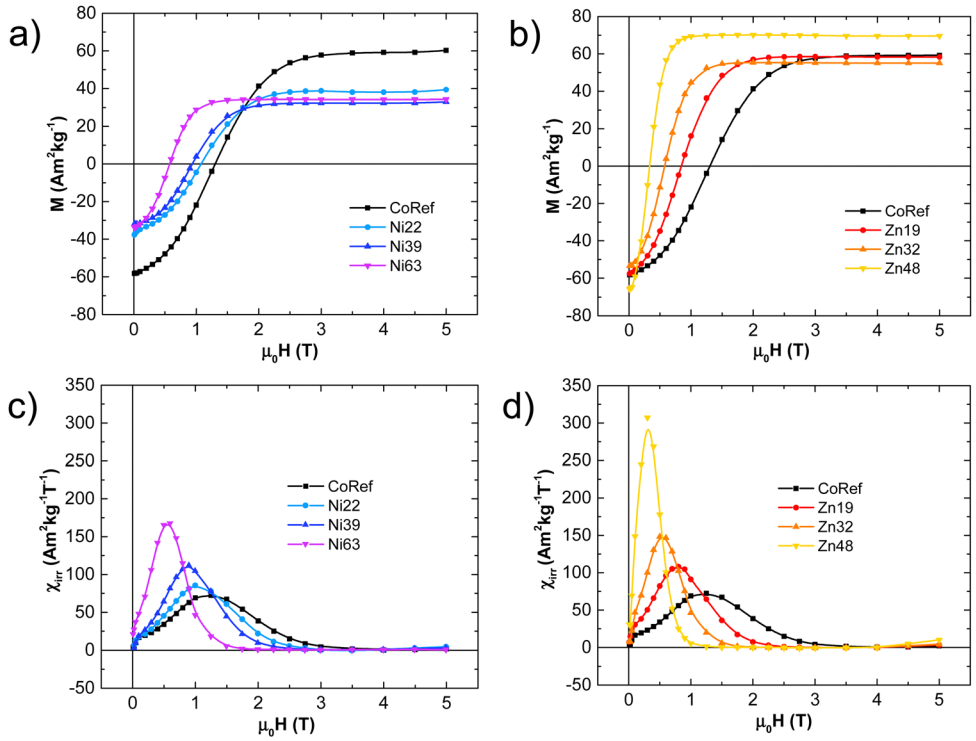

Fig. 2 (a) and (b) DCD remanence plots and (c) and (d) switching field distributions (SFD) for the Zn and the Ni-series.

reversal. Both Ni^{2+} and Zn^{2+} have the same qualitative effect on the SFD, lowering their maximum position ($\mu_0 H_{sw}$) as shown in Table 2. The effect is more marked for Zn^{2+}, since twice more Ni^{2+} is needed to have $\mu_0 H_{sw}$ dropping to 0.6 T; the same applies to the width of the SFDs, showing that the substitution with Zn^{2+} narrows down the SFD more significantly than that with Ni^{2+}.

Further evidence can be found in hysteresis loops at 5 K (Fig. 4), where the coercivity, $\mu_0 H_c$, monotonically decreases as the Zn^{2+}/Ni^{2+} content increases; the $\mu_0 H_c$ values of both series are similar to the corresponding $\mu_0 H_{sw}$. (Table 2). An estimation of the NPs' magnetic anisotropy was obtained by:[43]

$$K_a = \frac{\mu_0 H_K M_s}{2} \quad (1)$$

where H_K is the anisotropy field of the material. Kodama *et al.*[44] pointed out that $\mu_0 H_K \sim \mu_0 H_{irr}$, where $\mu_0 H_{irr}$ is calculated as the field where the difference between the magnetizing and the demagnetizing branches of the hysteresis loop curve reaches 1%.[45] The K_a values are reported in Table 2, and their magnitude is similar to those reported in the literature.[28]

Spinel ferrites have a cubic magneto-crystalline anisotropy with an expected reduced remanent magnetization (M_r/M_s) of $\sim$ 0.83–0.87,[46] but this feature is usually suppressed in small NPs by the surface and shape contributions, resulting in a uniaxial effective anisotropy; this is confirmed by the low M_r/M_s value of $\sim$0.5, characteristic for uniaxial anisotropy.[40,42] In our case, the undoped cobalt ferrite sample CoRef possesses a M_r/M_s value of approximately 0.6, confirming the presence of competing uniaxial and cubic anisotropy contributions. Interestingly, the substitution with Ni^{2+} cations, with lower single-ion anisotropy, compared to Co^{2+} initially leads to an increase in M_r/M_s, while one would expect a reduction due to the decrease in a cubic magneto-crystalline term. This can be attributed to the change in cationic distribution. In fact, the inversion degree for nickel ferrite is expected to be higher than

that for cobalt ferrite;[13] that can result in an increase in cobalt occupying octahedral sites where it significantly contributes to anisotropy.[47] Alternatively, Ni^{2+} cations may lower the surface anisotropy term, thereby reducing this source of uniaxial anisotropy. At the same time, as expected, the introduction of Zn^{2+} led to the formation of a pronounced uniaxial anisotropy, with M_r/M_s tending to be 0.5.[42]

Magnetic interparticle interactions

To study NPs' magnetic interparticle interactions, normalized IRM and DCD magnetizations can be compared by means of the Kelly equation, providing the so-called δm-plot:[48,49]

$$\delta m = m_{DCD}(H) - 1 + 2m_{IRM}(H) \quad (2)$$

The prevalence of either dipolar or superexchange interactions can be evaluated on the basis of the negative/positive dips, respectively,[50] although some contribution of the intraparticle effect can be present[51,52] Since the NPs are physically separated by an OLAC layer, only dipolar interactions are expected. The increase of Ni^{2+} and Zn^{2+} substitution shifts the average reversal field (*i.e.*, the peak position) to lower values—in agreement with the coercivities and SFD peaks. In the case of Zn^{2+}, the substitution also causes a remarkable increase in peak depth, indicating an increase in interaction strength.

A semi-quantitative estimation of the magnetic dipolar interactions can be obtained by calculating the dipolar energy.[53] In general, a system of randomly distributed NPs with average magnetic moment μ and average separation d, the dipole–dipole interaction energy among particles can be expressed as follows:

$$\langle E_{dip} \rangle \cong \frac{\mu_0 \langle \mu^2 \rangle}{4\pi d^3} = \frac{\mu_0 M_s^2 \rho^2 \langle V^2 \rangle}{4\pi d^3} \quad (3)$$

where ρ is the volume density of the material (estimated to be 5290 kg m^{-3} for all samples[12]), $\langle V^2 \rangle$ is the average volume calculated by considering all particles as spherical, and d is the average center-to-center distance of two nanoparticles covered with a single layer of OLAC molecules 2 nm long.[45,54,55] Fig. 3c and d show that E_{dip} and δm dip depth follow the same overall trend, confirming our interpretation. The small variation in M_s due to the introduction of Ni^{2+} is expected to be reflected in small variations in the dipolar interactions, which are indeed observed. This is in agreement with literature comparing cobalt and nickel ferrites.[52] Both trends of interactions measured in the case of the Zn-series are qualitatively matching. The accordance between the two methods lends robustness to the measure of the dip depth in δm plots, offering reliable means of assessing magnetic interactions among nanoparticles.

Saturation magnetization

Finally, it is quite interesting to discuss the trend of M_s with respect to the chemical composition of the samples (ESI,† Section S7). In the case of the Ni-series, Ni^{2+} induces a steep decrease in M_s followed by an almost constant trend, leaving little room for property tuning (Fig. 4 and Table 2). The Ni^{2+} spin-only magnetic moment of $2\mu_B$ is the lowest of all ions, and its selectivity drives it to O_h-sites, decreasing the $\sum \mu_{O_h}$ term and explaining our observations. The moderate entity of the effect is in accordance with the literature.[28,32,56,57]

Increasing Zn^{2+}, instead, reveals a monotonic increase in M_s at 5 K, inducing an increase in M_s from ~103 A m^2 kg^{-1} for $x = 0$ to ~143 A m^2 kg^{-1} for $x = 0.48$ (Fig. 4 and Table 2). The Zn^{2+} diamagnetism and the selectivity for T_d-sites[27,58] make it decrease the term $\sum \mu_{T_d}$, unbalancing the sum of the moments and increasing saturation. However, the increase in saturation

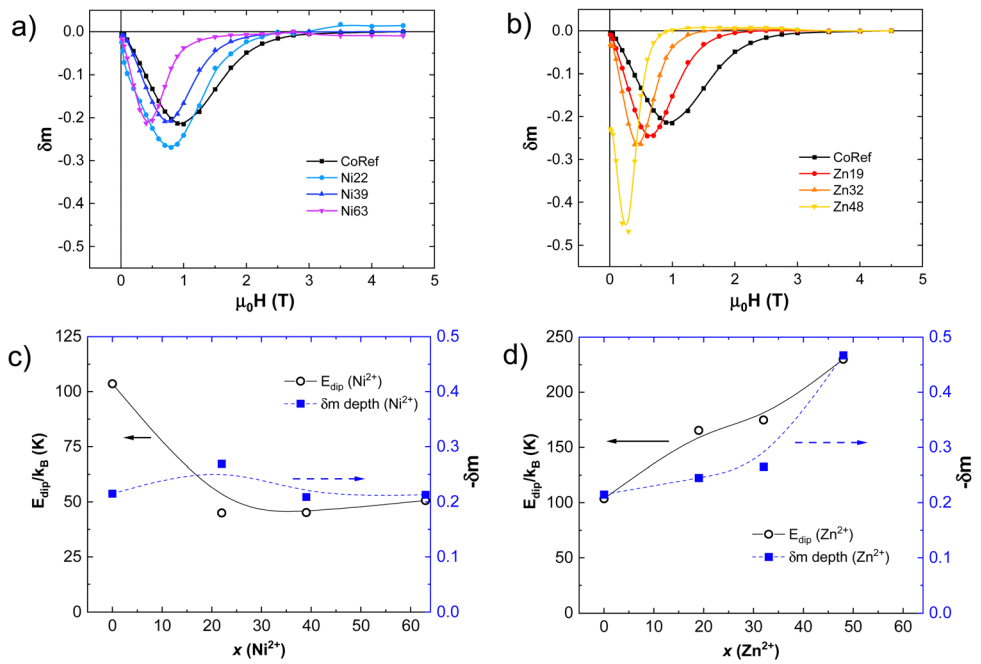

Fig. 3 (a) and (b) interaction δm plots of Ni-series and Zn-series, and (c) and (d) interaction dipolar energy values compared with δm profile depth.

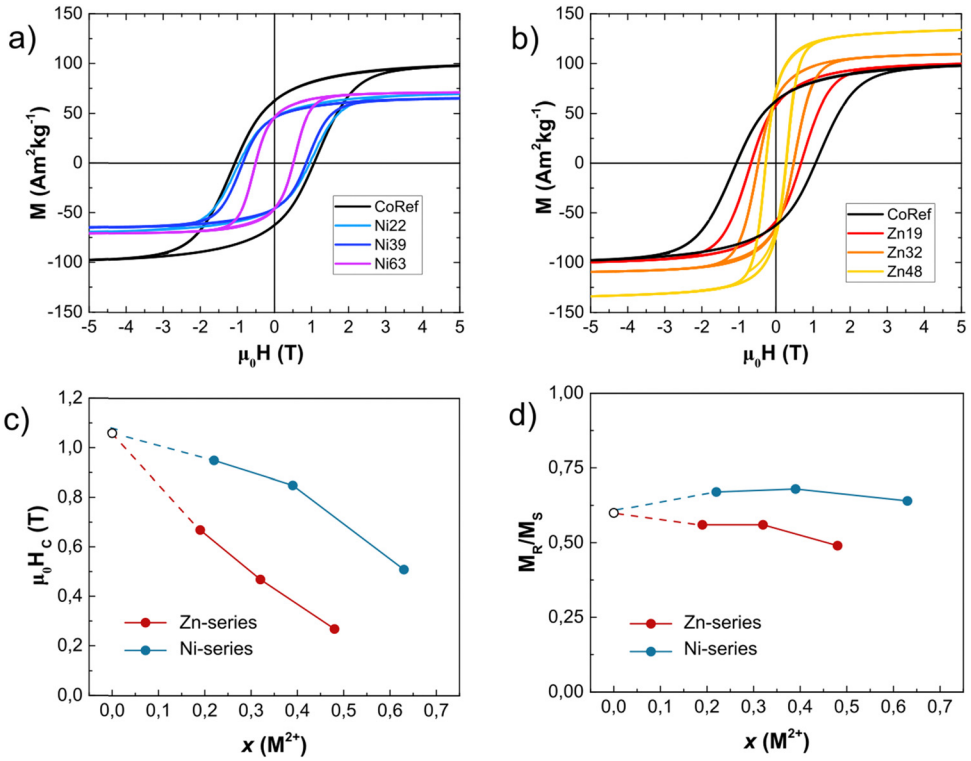

Fig. 4 (a) and (b) 5 K isothermal magnetization plots for Ni and Zn-series; (c) coercivity and (d) reduced remanent magnetization (M_r/M_s) for all samples.

with Zn^{2+} content is limited to $Zn^{2+} \sim 0.5$:[26,42] due to its diamagnetic nature, it cannot participate in super-exchange interactions, interrupting the magnetic superexchange coupling and weakening the magnetic structure of the material. Above this threshold, the magnetic behaviour converges to that of $ZnFe_2O_4$,[59,60] a normal antiferromagnetic spinel (T_N = 10 K),[13] and thus M_s decreases. Our results are in qualitative agreement with this explanation and with other results obtained by TD.[26,42]

The M_s values can be estimated using the two-sublattice Néel model, considering the well-known ion site selectivity of Ni^{2+} for O_h-sites[56] and of Zn^{2+} for T_d-sites[27] and the spin-only magnetic moment of our metal cations ($Zn^{2+} = 0\mu_B$, $Co^{2+} = 3\mu_B$, $Ni^{2+} = 2\mu_B$, $Fe^{3+} = 5\mu_B$).[12] For both series, an equation was written to express M_s as a function of the stoichiometric coefficient of M^{2+} (x) and the one of Co^{2+} in O_h-sites (y, corresponding to δ). For the Ni-series, the expression of the Bohr magneton magnetization per formula unit is (ESI,† Section S7)

$$\mu_{fu}^{Ni}(x,y) = 7 - 5x - 4y, \quad (4)$$

while for the Zn-series, the expression is

$$\mu_{fu}^{Zn}(x,y) = 7 + 3x - 4y \quad (5)$$

Note that the stoichiometric coefficient of Fe is kept to 2. Assuming that all the M^{2+} cations occupy their preferential sites, the functions can be plotted as $M_s(x,y)$ maps (Fig. 5), allowing us to easily predict M_s for different x and y. Reciprocally, an estimate of the cationic distribution (*i.e.*, y) can be obtained if M_s and x are known. The excluded grey areas are present because $x + y$ cannot be greater than 1.

Considering CoRef, cobalt ferrite is a partially inverted spinel, meaning that a fraction of Co^{2+} is still in T_d-sites; far from the intention of giving an exact value of the cation distribution, the position of the point in the graph suggests $y \sim 0.66$, which is close to literature values.[13,16–18]

The calculation explains a small change in magnetic saturation for the Ni-series after Ni22, with the points arranged between two iso-composition lines. The common O_h-site selectivity of Co^{2+} and Ni^{2+} implies that with increasing substitution, if Ni^{2+} simply replaces Co^{2+} at O_h sites, the magnetization will reduce slowly due to the small difference in spin-only magnetic moment between the two cations.

Turning now to the Zn series, Zn19 lies almost on the same iso-magnetization line of CoRef, thus suggesting an increase in the *relative* cobalt fraction in O_h-sites ($y \sim 0.8$). This is consistent with the almost identical saturation of CoRef and Zn19, and it is in accordance with the fact that Zn^{2+} being T_d-site selective, should occupy the fraction of T_d-sites which would be filled by Co^{2+} in $CoFe_2O_4$. Zn32 and Zn48 experimental values are lower than the value predicted for their composition, lying on the composition limit line. This discrepancy may reflect spin canting, size effects, and a small Zn^{2+} quantity in O_h-sites. Compared to other synthetic methods,[14,59–62] TD gives nanoparticles among those with the highest M_s values.[63,64] The differences are certainly related to the cationic distribution,[41] size distribution, spin canting and surface layer.[65]

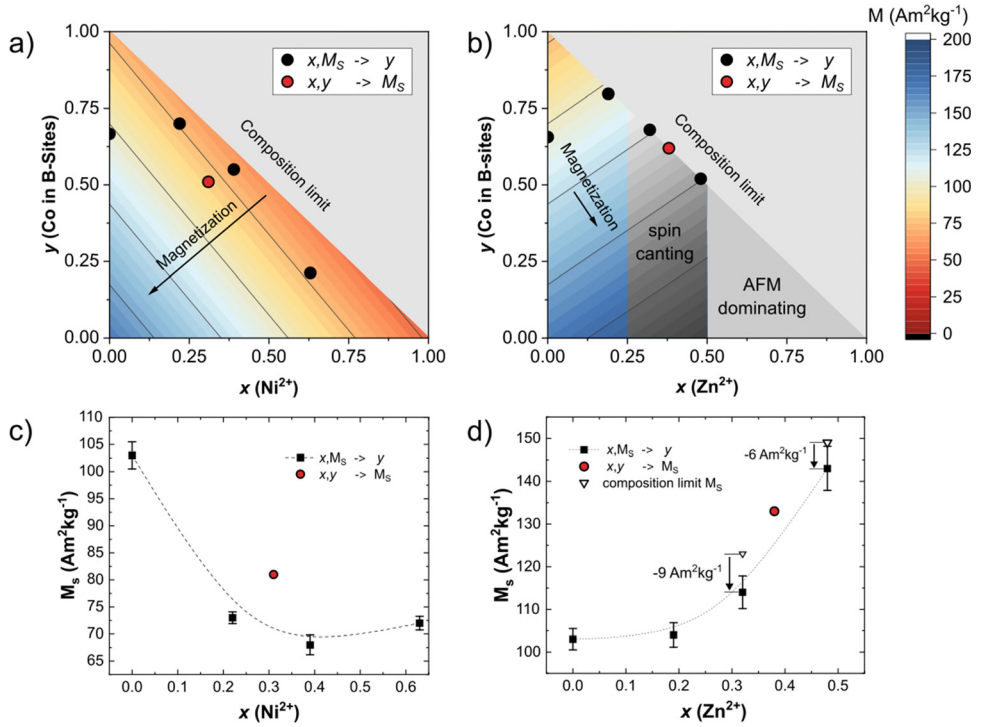

Fig. 5 (a) and (b) Low temperature magnetization maps calculated as a function of M^{2+} stoichiometric coefficient (x) and Co^{2+} inversion degree (y) for (a) Ni- and (b) Zn-series. Black dots represent the experimental saturations from hysteresis loops, while red dots represent M_s obtained from two additional samples with known composition and cationic distribution (Mössbauer spectroscopy data, see the ESI†). The black arrow indicates the verse of increasing magnetization. The (c) and (d) graphs compare the experimental and calculated magnetizations with respect to the composition for Ni- and Zn-series. Triangles indicate the maximal M_s value possible for two compositions with low M_s, as indicated on the map.

To confirm the usefulness of the $M_s(x,y)$ maps, the cationic distribution of samples of similar composition (Ni31 and Zn38) has been determined by Mössbauer spectrometry at 12 K and under an intense magnetic field of 8 T (ESI,† Section S8), yielding y = 0.54 and 0.62, respectively.

Combining x and y values yields M_s which is found to be close to the expected values (see ESI†). Yet, the obtained values are smaller, as mentioned earlier. This stems from structural features (defects, surface contributions) and the possible effect of the ligand on the magnetic moments on the surface.[65]

Furthermore, by examining Fig. S1 (ESI†), we note that only the samples obtained by this TD synthesis come close to the spin-only M_s, while other synthesis methods provide M_s much lower than any values predicted by the map, regardless of the particle size. As shown in Fig. S1 (ESI†), M_s depends greatly on the synthesis methods for a given x. $M_s(x,y)$ maps may be used to give a quick graphical estimate of whether these differences stem from different δ and thus providing a simple way to compare synthetic methods.

Conclusions

The magnetic properties of two sets of Ni^{2+} and Zn^{2+} doped cobalt ferrite NPs with equal size of ~9 nm were investigated to evaluate the influence of cation distribution over chemical composition on the saturation magnetization, magnetic anisotropy and interparticle interactions. Specifically, we observed up to 40% enhancement of saturation magnetization and decreased magnetic anisotropy in samples with greater Zn^{2+} content. The highest value of saturation magnetisation of 143 ± 5 A m^2 kg^{-1} at 5 K, which is 40% higher than in the CoRef sample, was found for a sample with the composition $Zn_{0.48}Co_{0.26}Fe_{2.26}O_4$. In contrast, Ni^{2+} substitution resulted in a decrease in both magnetization by ~30% and anisotropy by ~70% for the higher concentration of nickel.

A strong correlation was found between the results from the δm plot and the calculated dipolar energy. The obtained results suggest that Zn^{2+} substitution strongly affects the dipolar interparticle interaction intensity due to the increasing saturation magnetization and decreasing magnetocrystalline anisotropy.

Moreover, the inversion/doping content maps developed in this study provide a simple method to both visualize substitution impacts and predict M_s values from knowledge of only cation distributions or compositions. Our demonstration of accurate modelling of experimental data highlights the utility of these maps for the rational design of spinel ferrite nanoparticles tailored to further application needs.

Author contributions

The paper and ESI were written based on the contributions of all authors. P. M., D. P., F. C. and R. M. designed the

experiments; R. M., A. O. and D. P. coordinated the data analysis and discussion. M. B. and P. M. synthesized the nanoparticles and characterized them by XRPD and magnetometry techniques. G. B. performed structural characterisation by TEM. N. Y. performed Mössbauer spectrometry. All authors contributed to the results discussion and revision of the article.

Conflicts of interest

There are no conflicts to declare.

Acknowledgements

P. M. and R. M. thank the Swedish Energy Agency (project number 46561-1) and the Swedish Research Council (VR). D. P. acknowledges project code PE0000021, Concession Decree No. 1561 of 11.10.2022 adopted by the ''Ministero dell'Università e della Ricerca (MUR)'', according to attachment E of Decree No. 1561/2022, Project title ''Network 4 Energy Sustainable Transition-NEST'' in the frame of study of surface wettability properties, and REMAP, which has received funding from the European Commission PathFinder open programme under grant agreement No. 101046909.

Notes and references

1 N. Lee, D. Yoo, D. Ling, M. H. Cho, T. Hyeon and J. Cheon, Iron Oxide Based Nanoparticles for Multimodal Imaging and Magnetoresponsive Therapy, *Chem. Rev.*, 2015, **115**, 10637–10689.

2 J. Jang, H. Nah, J.-H. Lee, S. H. Moon, M. G. Kim and J. Cheon, Critical Enhancements of MRI Contrast and Hyperthermic Effects by Dopant-Controlled Magnetic Nanoparticles, *Angew. Chem., Int. Ed.*, 2009, **48**, 1234–1238.

3 S. H. Koenig and K. E. Kellar, Theory of 1/T 1 and 1/T 2 NMRD profiles of solutions of magnetic nanoparticles, *Magn. Reson. Med.*, 1995, **34**, 227–233.

4 M. Colombo, S. Carregal-Romero, M. F. Casula, L. Gutiérrez, M. P. Morales, I. B. Böhm, J. T. Heverhagen, D. Prosperi and W. J. Parak, Biological applications of magnetic nanoparticles, *Chem. Soc. Rev.*, 2012, **41**, 4306–4334.

5 N. Sanpo, C. C. Berndt, C. Wen and J. Wang, Transition metal-substituted cobalt ferrite nanoparticles for biomedical applications, *Acta Biomater.*, 2013, **9**, 5830–5837.

6 P. Maltoni, T. Sarkar, G. Barucca, G. Varvaro, D. Peddis and R. Mathieu, Exploring the magnetic properties and magnetic coupling in $SrFe_{12}O_{19}/Co_{1-x}Zn_xFe_2O_4$ nanocomposites, *J. Magn. Magn. Mater.*, 2021, **535**, 168095.

7 M. Estrader, A. López-Ortega, S. Estradé, I. V. Golosovsky, G. Salazar-Alvarez, M. Vasilakaki, K. N. Trohidou, M. Varela, D. C. Stanley, M. Sinko, M. J. Pechan, D. J. Keavney, F. Peiró, S. Suriñach, M. D. Baró and J. Nogués, Robust antiferromagnetic coupling in hard-soft bi-magnetic core/shell nanoparticles, *Nat. Commun.*, 2013, **4**, 2960.

8 P. Shyam, M. Mørch, A. Z. Eikeland, J. Ahlburg, A. Mamakhel, M. Saura-Múzquiz and M. Christensen, Combined characterization approaches to investigate magnetostructural effects in exchange-spring ferrite nanocomposite magnets, *Mater. Chem. Front.*, 2022, **6**, 2422–2437.

9 B. Muzzi, M. Albino, M. Petrecca, C. Innocenti, C. de, J. Fernández, G. Bertoni, C. Marquina, M. R. Ibarra and C. Sangregorio, 3d Metal Doping of Core@Shell Wüstite@ ferrite Nanoparticles as a Promising Route toward Room Temperature Exchange Bias Magnets, *Small*, 2022, **18**, 1–11.

10 R. Sharma, P. Thakur, P. Sharma and V. Sharma, Ferrimagnetic Ni2+ doped Mg-Zn spinel ferrite nanoparticles for high density information storage, *J. Alloys Compd.*, 2017, **704**, 7–17.

11 P. Maltoni, M. Baričić, G. Barucca, M. C. Spadaro, J. Arbiol, N. Yaacoub, D. Peddis and R. Mathieu, Tunable particle-agglomeration and magnetic coupling in bi-magnetic nanocomposites, *Phys. Chem. Chem. Phys.*, 2023, **25**, 27817–27828.

12 B. D. Cullity and C. D. Graham, *Introduction to Magnetic Materials*, John Wiley & Sons, Inc., Hoboken, NJ, USA, 2008.

13 F. G. da Silva, J. Depeyrot, A. F. C. Campos, R. Aquino, D. Fiorani and D. Peddis, Structural and Magnetic Properties of Spinel Ferrite Nanoparticles, *J. Nanosci. Nanotechnol.*, 2019, **19**, 4888–4902.

14 S. S. Jadhav, S. E. Shirsath, S. M. Patange and K. M. Jadhav, Effect of Zn substitution on magnetic properties of nanocrystalline cobalt ferrite, *J. Appl. Phys.*, 2010, **108**, 093920.

15 A. Feirweather, F. F. Roberts and A. J. E. Welch, Ferrites, *Rep. Prog. Phys.*, 1952, **15**, 142–172.

16 D. Carta, M. F. Casula, A. Falqui, D. Loche, G. Mountjoy, C. Sangregorio and A. Corrias, A Structural and Magnetic Investigation of the Inversion Degree in Ferrite Nanocrystals MFe_2O_4 (M = Mn, Co, Ni), *J. Phys. Chem. C*, 2009, **113**, 8606–8615.

17 A. S. Vaingankar, B. V. Khasbardar and R. N. Patil, X-ray spectroscopic study of cobalt ferrite, *J. Phys. F: Met. Phys.*, 1980, **10**, 1615–1619.

18 D. Carta, G. Mountjoy, G. Navarra, M. F. Casula, D. Loche, S. Marras and A. Corrias, X-ray Absorption Investigation of the Formation of Cobalt Ferrite Nanoparticles in an Aerogel Silica Matrix, *J. Phys. Chem. C*, 2008, **112**, 19791.

19 H. L. Andersen, M. Saura-Múzquiz, C. Granados-Miralles, E. Canévet, N. Lock and M. Christensen, Crystalline and magnetic structure-property relationship in spinel ferrite nanoparticles, *Nanoscale*, 2018, **10**, 14902–14914.

20 J. M. D. Coey, *Magnetism and Magnetic Materials*, Cambridge University Press, Cambridge, 2010.

21 S. Chikazumi and C. D. Graham, Magnetocrystalline anisotropy, *Physics of Ferromagnetism*, International series of monographs on physics, Oxford University Press, New York, 2nd edn, 1997, ch. 12, pp. 270–272.

22 G. Varvaro, A. Omelyanchik and D. Peddis, *Tailored Functional Oxide Nanomaterials*, Wiley, 2022, pp. 405–437.

23 G. F. Dionne, *Magnetic Oxides*, Springer US, Boston, MA, 2009, vol. 8.

24 K. R. Sanchez-Lievanos, J. L. Stair and K. E. Knowles, Cation Distribution in Spinel Ferrite Nanocrystals: Characterization,

Impact on their Physical Properties, and Opportunities for Synthetic Control, *Inorg. Chem.*, 2021, **60**, 4291–4305.
25 D. Peddis, in *Magnetic Nanoparticle Assemblies*, ed. K. N. Trohidou, Pan Stanford, Singapore, 2014, vol. 7, pp. 159–198.
26 V. Mameli, A. Musinu, A. Ardu, G. Ennas, D. Peddis, D. Niznansky, C. Sangregorio, C. Innocenti, N. T. K. Thanh and C. Cannas, Studying the effect of Zn-substitution on the magnetic and hyperthermic properties of cobalt ferrite nanoparticles, *Nanoscale*, 2016, **8**, 10124–10137.
27 H. L. Andersen, C. Granados-Miralles, M. Saura-Múzquiz, M. Stingaciu, J. Larsen, F. Søndergaard-Pedersen, J. V. Ahlburg, L. Keller, C. Frandsen and M. Christensen, Enhanced intrinsic saturation magnetization of Zn_xCo_{1-x}-Fe_2O_4 nanocrystallites with metastable spinel inversion, *Mater. Chem. Front.*, 2019, **3**, 668–679.
28 G. Muscas, N. Yaacoub, G. Concas, F. Sayed, R. Sayed Hassan, J. M. Greneche, C. Cannas, A. Musinu, V. Foglietti, S. Casciardi, C. Sangregorio and D. Peddis, Evolution of the magnetic structure with chemical composition in spinel iron oxide nanoparticles, *Nanoscale*, 2015, **7**, 13576–13585.
29 S. Sun, H. Zeng, D. B. Robinson, S. Raoux, P. M. Rice, S. X. Wang and G. Li, Monodisperse MFe_2O_4 (M = Fe, Co, Mn) Nanoparticles, *J. Am. Chem. Soc.*, 2004, **126**, 273–279.
30 U. B. Sontu, N. G. Rao, F. C. Chou and V. M. Ramana Reddy, Temperature dependent and applied field strength dependent magnetic study of cobalt nickel ferrite nano particles: Synthesized by an environmentally benign method, *J. Magn. Magn. Mater.*, 2018, **452**, 398–406.
31 N. B. Velhal, N. D. Patil, A. R. Shelke, N. G. Deshpande and V. R. Puri, Structural, dielectric and magnetic properties of nickel substituted cobalt ferrite nanoparticles: Effect of nickel concentration, *AIP Adv.*, 2015, **5**, 097166.
32 T. Orlando, M. Albino, F. Orsini, C. Innocenti, M. Basini, P. Arosio, C. Sangregorio, M. Corti and A. Lascialfari, On the magnetic anisotropy and nuclear relaxivity effects of Co and Ni doping in iron oxide nanoparticles, *J. Appl. Phys.*, 2016, **119**, 134301.
33 A. B. Nawale, N. S. Kanhe, S. A. Raut, S. V. Bhoraskar, A. K. Das and V. L. Mathe, Investigation of structural, optical and magnetic properties of thermal plasma synthesized Ni-Co spinel ferrite nanoparticles, *Ceram. Int.*, 2017, **43**, 6637–6647.
34 G. Datt, M. Sen Bishwas, M. Manivel Raja and A. C. Abhyankar, Observation of magnetic anomalies in one-step solvothermally synthesized nickel-cobalt ferrite nanoparticles, *Nanoscale*, 2016, **8**, 5200–5213.
35 J. I. Langford and A. J. C. Wilson, Scherrer after sixty years: A survey and some new results in the determination of crystallite size, *J. Appl. Crystallogr.*, 2016, **11**, 1536–1545.
36 A. H. Morrish, *The Physical Principles of Magnetism*, IEEE Press, Piscataway, 1965, vol. 1.
37 G. Concas, F. Congiu, G. Muscas and D. Peddis, Determination of Blocking Temperature in Magnetization and Mössbauer Time Scale: A Functional Form Approach, *J. Phys. Chem. C*, 2017, **121**, 16541–16548.
38 D. Peddis, P. E. Jönsson, S. Laureti and G. Varvaro, in *Frontiers of Nanoscience*, ed. C. Binns, Elsevier B.V, Oxford, UK, 2014, vol. 6, pp. 129–188.
39 E. P. Wohlfarth, Relations between Different Modes of Acquisition of the Remanent Magnetization of Ferromagnetic Particles, *J. Appl. Phys.*, 1958, **29**, 595–596.
40 D. Peddis, C. Cannas, A. Musinu, A. Ardu, F. Orru, D. Fiorani, S. Laureti, D. Rinaldi, G. Muscas, G. Concas, G. Piccaluga, F. Orrù, D. Fiorani, S. Laureti, D. Rinaldi, G. Muscas, G. Concas and G. Piccaluga, Beyond the Effect of Particle Size: Influence of CoFe2O4 Nanoparticle Arrangements on Magnetic Properties, *Chem. Mater.*, 2013, **25**, 2005–2013.
41 S. Gyergyek, D. Makovec, A. Kodre, I. Arčon, M. Jagodič and M. Drofenik, Influence of synthesis method on structural and magnetic properties of cobalt ferrite nanoparticles, *J. Nanopart. Res.*, 2010, **12**, 1263–1273.
42 M. Albino, E. Fantechi, C. Innocenti, A. López-Ortega, V. Bonanni, G. Campo, F. Pineider, M. Gurioli, P. Arosio, T. Orlando, G. Bertoni, C. de Julián Fernández, A. Lascialfari and C. Sangregorio, Role of Zn^{2+} Substitution on the Magnetic, Hyperthermic, and Relaxometric Properties of Cobalt Ferrite Nanoparticles, *J. Phys. Chem. C*, 2019, **123**, 6148–6157.
43 S. Mørup, M. F. Hansen and C. Fradsen, *Magnetic Nanoparticles*, Amsterdam, 2011.
44 R. H. Kodama, A. E. Berkowitz, E. J. McNiff and S. Foner, Surface spin disorder in ferrite nanoparticles, *Phys. Rev. Lett.*, 1996, **77**, 394–397.
45 D. Peddis, F. Orrù, A. Ardu, C. Cannas, A. Musinu and G. Piccaluga, Interparticle Interactions and Magnetic Anisotropy in Cobalt Ferrite Nanoparticles: Influence of Molecular Coating, *Chem. Mater.*, 2012, **24**, 1062–1071.
46 S. E. Peschany and N. A. Usov, Theoretical hysteresis loops for single-domain particles with cubic anisotropy, *J. Magn. Magn. Mater.*, 1997, **174**, 247–260.
47 M. Tachiki, Origin of the Magnetic Anisotropy Energy of Cobalt Ferrite, *Prog. Theor. Phys.*, 1960, **23**, 1055–1072.
48 P. E. Kelly, K. O'Grady, P. I. Mayo and R. W. Chantrell, Switching mechanisms in cobalt-phosphorus thin films, *IEEE Trans. Magn.*, 1989, **25**, 3881–3883.
49 J. García-Otero, M. Porto and J. Rivas, Henkel plots of single-domain ferromagnetic particles, *J. Appl. Phys.*, 2000, **87**, 7376–7381.
50 C. Binns, *Nanomagnetism: Fundamentals and Applications*, Elsevier, 2014.
51 J. A. De Toro, M. Vasilakaki, S. S. Lee, M. S. Andersson, P. S. Normile, N. Yaacoub, P. Murray, E. H. Sánchez, P. Muñiz, D. Peddis, R. Mathieu, K. Liu, J. Geshev, K. N. Trohidou and J. Nogués, Remanence Plots as a Probe of Spin Disorder in Magnetic Nanoparticles, *Chem. Mater.*, 2017, **29**, 8258–8268.
52 A. Omelyanchik, S. Villa, M. Vasilakaki, G. Singh, A. M. Ferretti, A. Ponti, F. Canepa, G. Margaris, K. N. Trohidou and D. Peddis, Interplay between inter- and intraparticle interactions in bi-magnetic core/shell nanoparticles, *Nanoscale Adv.*, 2021, **3**, 6912–6924.

53 A. V. Ambarov, V. S. Zverev and E. A. Elfimova, Influence of field amplitude and dipolar interactions on the dynamic response of immobilized magnetic nanoparticles: Perpendicular mutual alignment of an alternating magnetic field and the easy axes, *Phys. Rev. E*, 2023, **107**, 24601.

54 G. Muscas, M. Cobianchi, A. Lascialfari, C. Cannas, A. Musinu, A. Omelyanchik, V. Rodionova, D. Fiorani, V. Mameli and D. Peddis, Magnetic Interactions Versus Magnetic Anisotropy in Spinel Ferrite Nanoparticles, *IEEE Magn. Lett.*, 2019, **10**, 1–5.

55 E. H. Sánchez, M. Vasilakaki, S. S. Lee, P. S. Normile, M. S. Andersson, R. Mathieu, A. López-Ortega, B. P. Pichon, D. Peddis, C. Binns, P. Nordblad, K. Trohidou, J. Nogués and J. A. De Toro, Crossover From Individual to Collective Magnetism in Dense Nanoparticle Systems: Local Anisotropy Versus Dipolar Interactions, *Small*, 2022, **18**, 2106762.

56 C. Yang, Y. Hu, X. Li, J. Li, L. Wang and H. Li, Tuning of magnetic properties and hyperfine interaction by the substitution of Ni^{2+} for cobalt ferrite nanoparticles, *J. Mater. Sci.: Mater. Electron.*, 2019, **30**, 19647–19653.

57 A. Omelyanchik, G. Singh, M. Volochaev, A. Sokolov, V. Rodionova and D. Peddis, Tunable magnetic properties of Ni-doped CoFe2O4 nanoparticles prepared by the sol–gel citrate self-combustion method, *J. Magn. Magn. Mater.*, 2019, **476**, 387–391.

58 S. Amiri and H. Shokrollahi, The role of cobalt ferrite magnetic nanoparticles in medical science, *Mater. Sci. Eng., C*, 2013, **33**, 1–8.

59 G. Barrera, M. Coisson, F. Celegato, S. Raghuvanshi, F. Mazaleyrat, S. N. Kane and P. Tiberto, Cation distribution effect on static and dynamic magnetic properties of Co1-xZnxFe2O4 ferrite powders, *J. Magn. Magn. Mater.*, 2018, **456**, 372–380.

60 A. Omelyanchik, K. Levada, S. Pshenichnikov, M. Abdolrahim, M. Baricic, A. Kapitunova, A. Galieva, S. Sukhikh, L. Astakhova, S. Antipov, B. Fabiano, D. Peddis and V. Rodionova, Green Synthesis of Co-Zn Spinel Ferrite Nanoparticles: Magnetic and Intrinsic Antimicrobial Properties, *Materials*, 2020, **13**, 5014.

61 D. D. Andhare, S. R. Patade, J. S. Kounsalye and K. M. Jadhav, Effect of Zn doping on structural, magnetic and optical properties of cobalt ferrite nanoparticles synthesized *via*. Co-precipitation method, *Phys. B*, 2020, **583**, 412051.

62 M. Stefanescu, M. Bozdog, C. Muntean, O. Stefanescu and T. Vlase, Synthesis and magnetic properties of $Co_{1-x}Zn_x$-Fe_2O_4 ($x = 0 \div 1$) nanopowders by thermal decomposition of Co(II), Zn(II) and Fe(III) carboxylates, *J. Magn. Magn. Mater.*, 2015, **393**, 92–98.

63 G. Muscas, S. Jovanović, M. Vukomanović, M. Spreitzer and D. Peddis, Zn-doped cobalt ferrite: Tuning the interactions by chemical composition, *J. Alloys Compd.*, 2019, **796**, 203–209.

64 R. Topkaya, A. Baykal and A. Demir, Yafet–Kittel-type magnetic order in Zn-substituted cobalt ferrite nanoparticles with uniaxial anisotropy, *J. Nanopart. Res.*, 2013, **15**, 1359.

65 C. R. Vestal and Z. J. Zhang, Effects of Surface Coordination Chemistry on the Magnetic Properties of $MnFe_2O_4$ Spinel Ferrite Nanoparticles, *J. Am. Chem. Soc.*, 2003, **125**, 9828–9833.

